

# Energy Transport and its Function in Heptahelical Transmembrane Proteins

Nadja Helmer,<sup>1</sup> Steffen Wolf,<sup>1</sup> and Gerhard Stock<sup>1, a)</sup>

*Biomolecular Dynamics, Institute of Physics, University of Freiburg, 79104 Freiburg, Germany*

(Dated: 14 October 2022)

Photoproteins such as bacteriorhodopsin (bR) and rhodopsin (Rho) need to effectively dissipate photoinduced excess energy to prevent themselves from damage. Another well-studied 7 transmembrane (TM) helices protein is the  $\beta_2$  adrenergic receptor ( $\beta_2$ AR), a G protein-coupled receptor (GPCR) for which energy dissipation paths have been linked with allosteric communication. To study the vibrational energy transport in the active and inactive states of these proteins, a master equation approach [J. Chem. Phys. **152**, 045103 (2020)] is employed, which uses scaling rules that allow to calculate energy transport rates solely based on the protein structure. Despite their overall structural similarities, the three 7TM proteins reveal quite different strategies to redistribute excess energy. While bR quickly removes the energy using the TM7 helix as a 'lightning rod', Rho exhibits a rather poor energy dissipation, which might eventually require the hydrolysis of the Schiff base between the protein and the retinal chromophore to prevent overheating. Heating the ligand adrenaline of  $\beta_2$ AR, the resulting energy transport network of the protein is found to change significantly upon switching from the active to the inactive state. While the energy flow may highlight aspects of the interresidue couplings of  $\beta_2$ AR, it seems not particularly suited to explain allosteric phenomena.

## INTRODUCTION

Vibrational energy transport can be a critical aspect of protein functionality. In particular, proteins that employ or generate excess energy during their function need to quickly dissipate this energy to prevent damage to the protein.<sup>1</sup> For example, enzymatic reactions may release enough heat to unfold a protein.<sup>2</sup> Efficient energy dissipation is also crucial for photoproteins, which harness photonic energy via light-active cofactors, so-called chromophores, that can generate excess energies<sup>3</sup> even higher than 2 eV. Following photoexcitation, this is achieved via ultrafast internal conversion into the electronic ground state and subsequent redistribution of the chromophore vibrational energy into low-frequency modes.<sup>4</sup> Using time-resolved vibrational spectroscopy, the resulting flow of biomolecular energy along the protein backbone and via tertiary contacts such as hydrogen bonds, salt bridges and polar contacts can be monitored in space and time.<sup>5–10</sup> Notably, these energy transport pathways are believed to be linked to channels of allosteric communication,<sup>11–17</sup> which is of key importance for protein signaling and regulation.<sup>18</sup>

Well-known examples of photoproteins are the two protein families of microbial<sup>19–21</sup> and visual<sup>20,22</sup> rhodopsins. For the first family, the prime example is bacteriorhodopsin (bR),<sup>23</sup> which was discovered over 40 years ago as the only protein in the purple membrane of *Halobacterium salinarum*.<sup>24</sup> bR acts as light driven ion pump, using the energy of green light photons to pump protons out of a bacterial cell, creating a proton gradient for ATP production.<sup>25</sup> The visual rhodopsin family is best represented by rhodopsin (Rho) itself,

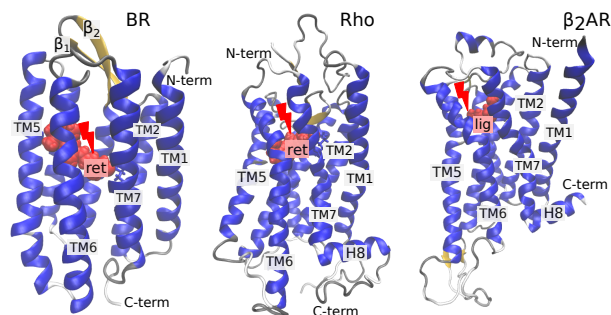


FIG. 1. Structure of the three molecular systems considered in this work: bacteriorhodopsin, rhodopsin, and  $\beta_2$  adrenergic receptor. To initiate nonequilibrium flow of vibrational energy, the chromophore retinal (in bR and Rho) or the ligand adrenaline (in  $\beta_2$ AR) is heated, which is indicated by a red flash of lightning.

which is the photoreceptive protein located in the membrane of vertebrate retina rod cells and forms a subgroup of the G protein-coupled receptor protein (GPCR) superfamily.<sup>26–28</sup> As can be seen in Fig. 1, both protein families share seven transmembrane helices (TM1–TM7) connected by intracellular loops (ICL) and extracellular loops (ECL) as well as a retinal chromophore bound to the protein core and covalently linked to the protein through a Schiff base via a lysine residue. Despite these global similarities, the details of the protein's architecture differ significantly, and both classes appear to have evolved independently.<sup>29</sup>

In both types of proteins, photon absorption induces an isomerization of retinal,<sup>20</sup> which drives protein conformational and electrostatic changes necessary for the protein's function. The main difference between bR and rhodopsin is found in the details of the photoreaction: bR undergoes a photocycle where the retinal starts in an

<sup>a)</sup>Electronic mail: stock@physik.uni-freiburg.de

*all-trans* configuration and isomerizes into a 13-*cis* arrangement, with the *all-trans* configuration and the initial protein conformation being restored at the end of the photo reaction. In Rho, the retinal starts in a 11-*cis* configuration and irreversibly converts into the *all-trans* state, switching the protein from an inactive dark state to the active Meta II state. The *all-trans* retinal then needs to be chemically cleaved from the protein and be chemically converted back into its 11-*cis* configuration by photoisomerases. Despite these differences,  $\sim 2/3$  of absorbed photons result in the isomerization in both bR and rhodopsin,<sup>20</sup> which in turn means that 1/3 of all absorbed photons inject their full energy into the protein via internal conversion, as fluorescence in both proteins is negligible.<sup>20,30</sup> Ultimately, only a part of the absorbed photonic energy is used to perform work,<sup>31</sup> while the rest is dissipated into the protein. Furthermore, the all-trans retinal in Meta II is chemically cleaved from the opsin apoprotein, unbinds from it and isomerizes back to 11-*cis* retinal using additional proteins.<sup>32,33</sup>

Apart from the photoprotein bR and Rho, we are also concerned with the  $\beta_2$  adrenergic receptor ( $\beta_2$ AR),<sup>27,34</sup> which represents a well-investigated GPCR that undergoes an allosteric transition upon ligand binding. As displayed in Fig. 1,  $\beta_2$ AR is structurally highly similar to Rho, but is activated by the diffusible ligand adrenaline instead of a chromophore. By heating the ligand and following the resulting energy flow through  $\beta_2$ AR, one may study the change of the energy transport network when we switch from the active to the inactive state. In this way we connect to recent work<sup>35</sup> that linked vibrational energy transport and allostery in  $\beta_2$ AR.

A number of approaches have been suggested to model protein energy flow based on molecular dynamics (MD) simulations.<sup>36–44</sup> Moreover, several authors have proposed network-type models,<sup>45–52</sup> which are derived, for instance, by computing the inter-residue energy flow to create an energy exchange network. To describe the energy transport in proteins between the different residues, Buchenberg et al. have proposed a master equation approach.<sup>49,51</sup> The discovery of scaling rules<sup>51,53</sup> allows for calculating the energy transport rates solely based on the protein structure. Hence, it can be applied on a single protein frame such as a crystal structure without the need for extensive MD simulations.

In this work, we use the master equation approach of Ref. 53 to study energy dissipation from retinal into both bR and Rho. Additionally, we consider the ligand-induced energy transport in  $\beta_2$ AR, in order to investigate a possible connection between energy dissipation paths and allostery. For all three proteins, high-resolution crystal structures are available in ground (inactive) states and active states.<sup>54–59</sup> For each system, we compute the energy transport rate matrix, which includes both transport along the backbone and through contacts. We evaluate a coarse-grained depiction of the rates on the level of the secondary structures, which yields an overview over the connectivity of the different proteins. By heating the

ligand or retinal, respectively, we visualize and discuss the resulting energy flow in some detail.

## THEORY AND METHODS

### Master Equation

Starting from a discretized diffusion equation, Buchenberg et al.<sup>51</sup> derived the energy flow master equation

$$\frac{dE_j(t)}{dt} = \sum_i [k_{ij}E_i(t) - k_{ji}E_j(t)], \quad (1)$$

where  $E_j$  describes the kinetic energy of residue  $j$  and  $k_{ij}$  denotes the transport rate from residue  $i$  to  $j$ . The corresponding energy transport times  $\tau_{ij}$  are obtained via  $\tau_{ij} = 1/k_{ij}$ . The rate matrix  $k_{ij}$  contains the full information about the energy redistribution, and can be employed to predict the energy evolution of the system. Moreover, one can consider the solvent as an additional state with solvent rates  $k_{ps}$  and  $k_{sp}$  from the protein into the solvent and back.<sup>38</sup> However, we do not include a solvent rate in this work, as the major protein surface is found at the membrane interface, and the protein-water interface above and below the membrane only leads to a non-specific removal of the excess heat.<sup>10,53</sup> Protein-membrane lipid contacts are mostly hydrophobic, and as was found earlier,<sup>44,51</sup> the energy transfer through such contacts can be safely neglected.

### Scaling rules and Identification of Contacts

The scaling rules of biomolecular energy flow allow to describe the energy transport in terms of only a few parameters, yielding a simple and transferable model. The scaling rule for backbone transport yields the rates<sup>51</sup>

$$k_{ij}^B = \frac{D_B}{\langle x_{ij} \rangle^2} \sqrt{\frac{f_j}{f_i}}, \quad (2)$$

and for contact transport we obtain<sup>53</sup>

$$k_{ij}^C = \frac{D_C}{\langle q_{ij} \rangle^2} \sqrt{\frac{f_j}{f_i}}. \quad (3)$$

Both rules follow from the diffusion equation with  $D_B$  and  $D_C$  being diffusion constants and  $f_i$  denoting the number of the degrees of freedom of residue  $i$ . In case of the backbone transport, we consider the average square distance  $\langle x_{ij} \rangle^2$  along covalent bonds between all atoms of residues  $i$  and  $j$ . In contrast to that, the contact transport only takes the atoms of selected contacts into account (see below) and is inversely proportional to the square mean distance  $\langle q_{ij} \rangle^2$  between those atoms. The diffusion constants were determined as  $D_B = 1.1 \text{ nm}^2\text{ps}^{-1}$  and  $D_C = 2.1 \times 10^{-3} \text{ nm}^2\text{ps}^{-1}$  in

Ref. 53 and serve as global constants, while the individual bond strength is reflected by  $\langle x_{ij} \rangle^2$  and  $\langle q_{ij} \rangle^2$ , respectively. The application of these scaling rules allow us to predict the energy transport directly from the connectivity within a protein structure, providing the general means to model the energy flow in various proteins using solely a crystal structure.

Since nonpolar contacts were shown to be negligible for energy transport,<sup>44,51</sup> they are omitted in this study. Moreover, as the residues that form strong polar contacts additionally also form hydrogen bonds (but with a smaller distance), it is sufficient to focus on hydrogen bonds for energy transport as a first approximation. Here we only include hydrogen bonds, where the distance between hydrogen atom and acceptor is smaller than 2.8 Å and the angle  $\theta$  between donor-acceptor-hydrogen is  $\theta \leq 30^\circ$ . Concerning ionic interactions in the considered proteins, charged residues interact with each other via salt bridges, i.e., combined ionic-hydrogen bond interactions. Hence, this type of interaction is already approximately taken care of via the hydrogen bond analysis. We furthermore consider ionic interactions over distances larger than 4.5 Å to be damped out by other residues found between them, and thus so weak that their contribution to energy transfer is negligible.

From these contacts, we compute the energy transport rates on the level of residues, as those are the states used in the master equation. To obtain a broader picture, we also consider the energy transport on the level of the protein’s secondary structures, where all rates between the residues of two secondary structures are combined into one rate. This method allows us to obtain a better overview of the connections between the different protein structures. The secondary structure rates can then be visualized in the protein structure to grasp the protein’s connectivity at one glance.

### Quantum Corrections

The above scaling rules were parameterized from classical nonequilibrium MD simulations.<sup>53</sup> However, classical mechanics approximate the quantum mechanics of anharmonic oscillators only well on short time scales.<sup>60–62</sup> In order to reproduce the correct energy transport time scales, it is thus necessary to introduce a quantum correction to our classical approach. As a simple approximation, it may be sufficient to rescale the diffusion coefficients  $D_B$  and  $D_C$  obtained from the classical MD simulations by a common quantum correction factor  $Q$ . By comparison of simulated and experimentally measured data for various test proteins, this factor was determined as  $Q = 3.1$  by Deniz et al.<sup>10</sup> As in this work we do not include the dissipation into the solvent water (which typically needs no correction<sup>38</sup>), the quantum correction is applied to all considered transport channels and therefore only serves as a general scaling factor to obtain the correct time scales.

### Structure Preparation

In order to compute the contact rates, we first have to identify the contacts that the protein forms. We apply our method to crystal structures, which were in part slightly modified. For bR, we base our calculations on the recently resolved set of crystal structures by Weinert et al.<sup>59</sup> We consider the inactive "dark" state (PDB 6RQP) with an *all-trans* retinal and the active state with 13-*cis* retinal (PDB 6RPH), which represents the subsequent N- and O-intermediates in the photocycle.<sup>23</sup> In this case, the crystal structures already include hydrogen atoms, which we use for further contact analysis. For Rho, we consider the inactive dark state (PDB 1U19), where the retinal is bound in the *cis* state, and the Meta II state (PDB 3PQR), with the isomerized retinal in the *all-trans* state still bound to the protein. The results for  $\beta_2$ AR relies on crystal structures of the inactive<sup>55</sup> (PDB 2RH1) and the active state<sup>57</sup> (PDB 3P0G) with the docked native ligand adrenaline. To verify that docking a ligand is a viable approach for studying energy transmission in proteins, we additionally considered a crystal structure of an active  $\beta_2$ AR-adrenaline complex<sup>63</sup> (PDB 4LDO). Missing hydrogen atoms are added to protein crystal structures with PROPKA<sup>64,65</sup> for a pH of 7 using the PDB2PQR web server.<sup>66,67</sup> The missing intracellular loop 3 in the  $\beta_2$ AR was recovered via the SWISS-MODEL web server,<sup>68</sup> and the native ligand adrenaline was added via docking using Autodock Vina.<sup>69</sup> T4 lysozyme fusion proteins and active state stabilizing peptides or proteins were removed. To handle the structural protein information, we use *MDAnalysis*.<sup>70,71</sup>

For MD simulations of  $\beta_2$ AR, the same structure preparation protocol was employed. In the case of the active receptor, we employed PDB structure 4LDO with the nanobody present to stabilize the receptor. The complex was embedded into a POPC lipid bilayer surrounded by water using INFLATEGRO2.<sup>72</sup>

### A. Molecular Dynamics Simulations

Atomic interactions were described by the Amber99SB\* force field<sup>73,74</sup> combined with the Berger lipid force field,<sup>75,76</sup> and the TIP3P water model.<sup>77</sup> Adrenaline parameters were generated using Antechamber<sup>78</sup> and Acyppe<sup>79</sup> with atomic parameters derived from GAFF parameters<sup>80</sup> and AM1-BCC atomic charges.<sup>81,82</sup>

Simulations were carried out using Gromacs v2018 (Ref. 83) in a CPU/GPU hybrid implementation. Van der Waals interactions were calculated with a cut-off of 1 nm, electrostatic interactions using the particle mesh Ewald method<sup>84</sup> with a minimal real-space cut-off of 1 nm. All covalent bonds with hydrogen atoms were constrained using LINCS.<sup>85</sup> After an initial steepest descent minimization with positional restraints of protein and ligand heavy atoms, an initial 10 ns equilibration MD simulation in the NPT ensemble was performed with a 2 fs time step and positional restraints of protein and ligand

heavy atoms. A temperature of 300 K was kept constant using the Nosé-Hoover thermostat<sup>86,87</sup> (coupling time constant of 0.2 ps), the pressure was kept constant at 1 bar using the Berendsen barostat<sup>88</sup> (coupling time constant of 0.5 ps) with semi-isotropic pressure coupling, followed by a second steepest descent minimisation without restraints and a short 0.1 ns equilibration MD simulation in the NPT ensemble. Then, 120 ns of free MD simulations were carried out, switching the barostat to the Parrinello-Rahman barostat.<sup>89</sup> Snapshots were collected each 20 ns, resulting in a total of 7 structures.

### Heating Process and Visualization

Performing extensive nonequilibrium MD simulations of the energy flow in proteins, Gulzar et al.<sup>43</sup> approximated the initial photoexcitation by an instantaneous temperature jump, where the resulting excess energy  $k_B\Delta T$  of the chromophore is chosen to match the  $S_0 \rightarrow S_1$  excitation energy of  $\approx 2$  eV, resulting in  $\Delta T \approx 600$  K. In the master equation simulations of the energy flow, we use this temperature change as initial condition at time  $t = 0$  to define the initial energy of the chosen heater system (i.e., retinal for bR and Rho and the ligand for  $\beta_2$ AR). We note that this choice does only affect the observed temperature scale but not the energy transfer dynamics of the master equation.

Solving the master equation (1) iteratively, we obtain the time evolution of the energy of every residue of the protein. To illustrate the energy transport in a more visual manner, we utilize these temperature curves to color the residues for each time step using *VMD*.<sup>90</sup> This visualization allows us to watch the energy distribution in form of a movie and choose suitable time frames for representation. In the end, the energy distributes until equilibrium is reached and the equipartition theorem is fulfilled.

## RESULTS

### Bacteriorhodopsin

Starting with bR, we find 34 contacts for the inactive state and 32 for the active state, which we list in Tab. S1. To analyze how the system deals with the energy of the absorbed photons, we heat the retinal chromophore, which is covalently bound to Lys216 in TM7.

After computing all contact and backbone rates, we group them according to the involved secondary structures. The resulting secondary structure contact rates can be found in Tab. I and Fig. 2. The rates provide a rough picture of the connectivity between the different parts of the protein. The two states mostly agree in connectivity and absolute value of the rates. Though the largest structural difference between both states is the outward motion of helices E and F<sup>59</sup> (here TM5 and TM6), the largest differences in the rates are found for

TABLE I. Secondary structure rates of bR for the active and inactive state. The rates are given in  $\text{ps}^{-1}$ .

Sec. Struct.		Rates	
Sec 1	Sec 2	Inactive	Active
N-term	TM2	0.26	0.11
TM1	$\beta_2$	0.26	0.16
TM1-TM2	C-term	0.09	
TM2	TM3	0.16	
TM2	TM7	0.16	0.15
TM2- $\beta_1$	TM3	0.14	0.10
$\beta_1$	$\beta_2$	0.75	0.46
TM3	TM7		0.11
TM3-TM4	TM5	0.21	
TM4	TM5	0.34	0.34
TM5	TM6	0.12	0.08
TM5	TM6-TM7	0.24	0.17
TM5-TM6	C-term	0.25	
TM6	TM7	0.15	0.10

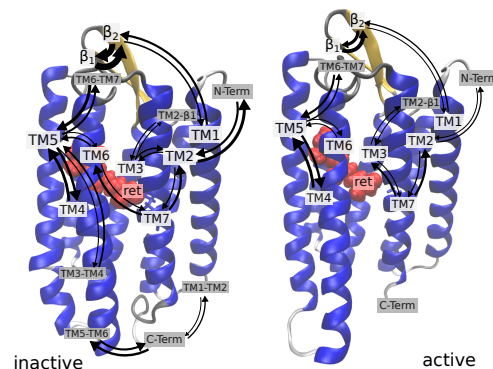


FIG. 2. Illustration of the secondary structure rates of bR as black arrows within a snapshot of the protein. The line width of the arrows are proportional to the rates. For each structure pair, the rates are shown in both directions.

helix G (here TM7). This is most likely due to the weakening of the Tyr185-Asp212 hydrogen bond, which elongates from 2.6 Å in the dark state to 3.1 Å in the active state. In general, there seem to be hardly any noticeable changes in the energy transport upon the activation of the protein. The main reason for this is that most contacts within the core of bR are hydrophobic and only a handful of contacts break during the photocycle. Furthermore, TM7 exhibits only two polar contacts via Asp204 and Asp212, hence energy transport via the backbone chain should dominate in both investigated structures.

Figure 3 shows both states of the system at 10 ps after heating the ligand impulsively (see Methods). As discussed above, the energy transport in the two states is very similar in behavior. We can observe that the energy flows through the covalent bond into TM7 and spreads in both directions from there. Additionally, TM3 and TM2 obtain small amounts of energy through contact

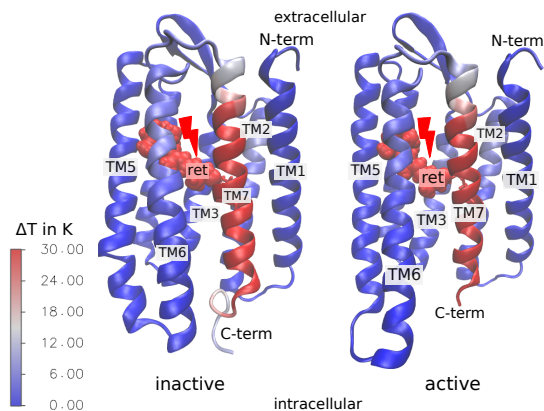


FIG. 3. BR at  $t = 10$  ps after heating the retinal. The left side shows the protein in the inactive state, the right side in the active state. Colors of the residues indicate the residue's temperature.

transport. However, as presumed, backbone transport strongly dominates. We note that the C-terminus of TM7 quickly receives a large amount of kinetic energy. In bR crystal structures, the 16 amino acid C-terminus is not resolved, and forms a random coil<sup>91</sup> that is embedded in the intracellular water bulk. Its removal does not affect the protein's folding and function as a proton pump,<sup>92</sup> but has been linked to protein stability.<sup>93</sup> Naturally, these amino acids will exhibit contacts with water molecules, and form an efficient position for dissipation of excess energy into the solvent. Figuratively speaking, the TM7 helix seems to act like a "lightning rod" providing a direct energy transfer path to the C-terminus, which forms a "grounding rod" to effectively dissipate excess energy into the solvent.

### Rhodopsin

We now turn to the analysis of energy transfer in Rho. We find 51 contacts between different residues for the dark state and 50 for the Meta II state, which are listed in Tab. S2. The secondary structure rates can be found in Tab. II with an illustration in Fig. 4. The inactive state contains slightly more internal connections and thus seems to be better at dissipating energy. Especially the two helices TM1 and TM7 are strongly connected with a large contact rate. In contrast to this, the active state appears to be more isolated, as many of the contacts break through changes in the structure upon activation.

As before we heat the retinal and observe how the energy distributes from there. Fig. 5 shows the two states of rhodopsin 10 ps after the heating process. The energy flows into TM7 through the covalent bond and quickly spreads in both directions along the backbone. However, the energy does not reach further than the ends of this helix. In the inactive state, we can additionally observe contact transport from TM7 into TM1 and TM3, even

TABLE II. Rates between the different secondary structures in Rho for both states. The rates are given in  $\text{ps}^{-1}$ .

Sec. Struct.		Rates	
Sec 1	Sec 2	Inactive	Active
N-Term	TM2		0.10
N-Term	ECL1	0.30	0.11
N-Term	ECL2	0.21	
N-Term	ECL3	0.16	
TM1	TM2	0.16	0.25
TM1	TM7	0.41	0.15
TM2	TM4	0.22	0.13
TM2	ECL2		0.27
TM3	ECL2	0.14	0.15
TM3	TM5	0.15	
TM3	TM6	0.18	
TM3	TM7	0.11	
TM4	TM5	0.35	0.49
ECL2	TM6	0.17	0.14
TM5	TM6		0.39
TM6	H8	0.10	
TM7	H8	0.17	

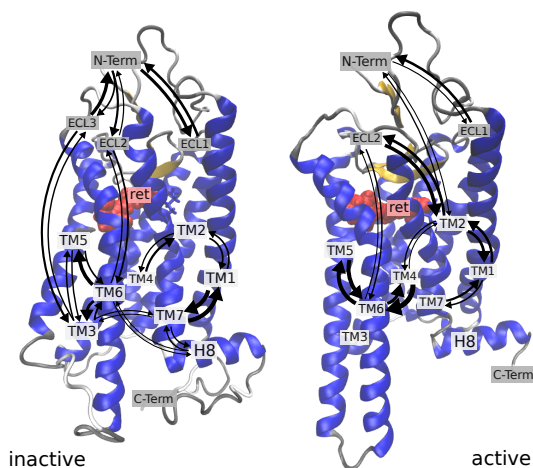


FIG. 4. Visualization of the secondary structures rates of Rho with black arrows indicating the energy transport between the structures. The arrow line width are proportional to the secondary structure rates.

though the energy flow towards TM3 seems negligible. The main path for this energy transfer is the salt bridge between the protonated Schiff base of the retinal and Glu113, which is a major structural feature to stabilize the dark state.<sup>94</sup> In the active state, on the other hand, no noticeable contact transport can be observed. This agrees with the lower connectivity we deduced from the rates.

In comparison with bR, we note that the excess energy is not quickly transferred to solvent-exposed unstructured domains, but remain in the core of the transmembrane helix bundle. In Rho, the C-terminus serves as important structural feature for signal transduction<sup>95</sup>

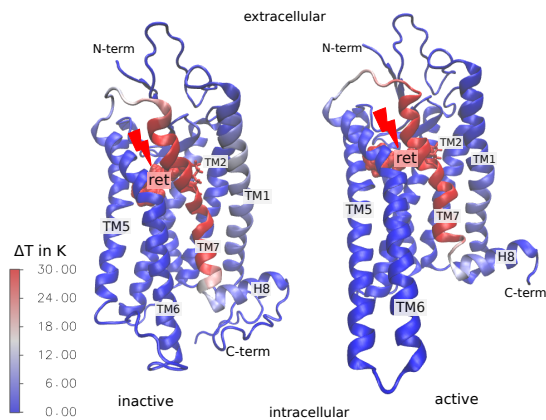


FIG. 5. Rho shown in both states at  $t = 10$  ps after heating the retinal. The heated retinal is indicated by a red lightning bolt. The coloration shows the local temperatures of residues.

and thus cannot serve as "grounding rod" as in bR. Instead, it appears that excess energy is distributed into the whole protein, and then slowly released from there to its environment. We notice that the salt bridge between the Schiff base and Glu113 ruptures only after retinal isomerization,<sup>20</sup> i.e., after the decay back into the retinal electronic ground state. Therefore, this salt bridge can indeed serve as energy dissipation channel. We finally note that the *all-trans* retinal in the active state still can absorb photons, which do not contribute to protein function anymore. Hydrolysis of the Schiff base on the formation of opsin may therefore not only serve for the reloading with 11-*cis* retinal, but also for the protection of rhodopsin from excess photon energy.

It has been shown that in both bR and Rho, protein-internal water molecules are essential for protein function and connect distant amino acid side chains to each other via hydrogen bonds.<sup>96</sup> We therefore tested for the example of Rho how much the treatment of water molecules observed in crystal structures as contact residues would contribute to energy transfer from the retinal to the protein. As shown in Tab. S3, we found a significant number of contacts with internal water molecules (37 in the inactive and 17 in the active state), however, the respective contact rates are mostly small. Hence, these water molecules represent dead ends for the energy transfer and do not significantly change the time-dependent energy distribution (Fig. S1). Protein-internal water molecules therefore are negligible for the overall energy transport in Rho.

### $\beta_2$ adrenergic receptor

Finally, we explore if the lessons learned from energy transfer in bR and Rho can be transferred to the energy transport in  $\beta_2$ AR. As stated before,  $\beta_2$ AR binds a ligand by forming polar and nonpolar contacts. In contrast to the other two systems, where the retinal was covalently bound to the protein and the energy entered the

protein through backbone transport along those bonds, here the energy flows into the protein through contact transport. Moreover, both states form at least 2 ligand contacts and the energy consequently already reaches different parts of the protein directly after the heating. The contacts formed with the ligand are shown in Fig. 6 and listed in Tab. III. In both states, the ligand binds to TM3 via a salt bridge / hydrogen bond combination with Asp113 and to TM7 via a bidentate hydrogen bond with Asn312. Additionally, the inactive state forms another contact through TM5 via Ser203, however, only with a small rate.

TABLE III. Rates of the contacts formed between the ligand adrenaline and  $\beta_2$ AR, given in  $\text{ps}^{-1}$ . "Adr" denotes adrenaline.

Residues		Rates	
Res 1	Res 2	Inactive	Active
Adr	Asp113	0.34	0.27
Adr	Ser203	0.12	
Adr	Asn312	0.14	0.14

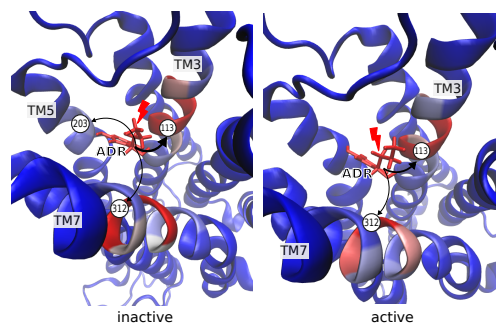


FIG. 6. Illustration of the contacts rates of  $\beta_2$ AR for the inactive state (left) and the active state (right).

From the contact analysis of  $\beta_2$ AR we find 61 contact rates in the inactive state and 50 in the active. This is a larger difference than in the two proteins before and already indicates that the protein has a higher connectivity before the activation. The contact rates are listed in Tab. S4. Considering the secondary structure rates displayed Fig. 7, the energy transport seems to completely change between the two states. A list of the rates can be found in in Tab. IV. Many of those changes involve TM5 and TM6, which are known for their outward movements when the protein transitions into the active state.<sup>57</sup>

In Fig. 8 we can find a snapshot of the protein 10 ps after heating the ligand. In both states, energy reaches TM3 and TM7 and travels in both directions along the backbone, respectively. In the active state, more energy reaches TM7. We can also see that some energy flows through the third contact in the inactive state to TM5, but only a minor amount compared to the other two he-

TABLE IV. Secondary structures in  $\beta_2$ AR shown for both states. The rates are given in  $\text{ps}^{-1}$ .

Sec. Struct.		Rates	
Sec 1	Sec 2	Inactive	Active
N-Term	ECL1		0.25
TM1	TM7	0.11	0.17
TM2	TM3	0.39	0.40
TM2	ECL2	0.15	
TM2	TM7	0.12	
ECL1	ECL2	0.11	
TM3	TM4		0.19
TM3	ECL2	0.71	0.11
TM3	TM5		0.17
TM3	TM7	0.18	0.28
ICL2	ICL3	0.18	
TM4	TM5		0.14
ECL2	TM7	0.24	0.26
TM5	TM6	0.29	0.19
TM6	TM7	0.19	0.54
TM6	ICL4	0.13	
TM7	H8	0.23	

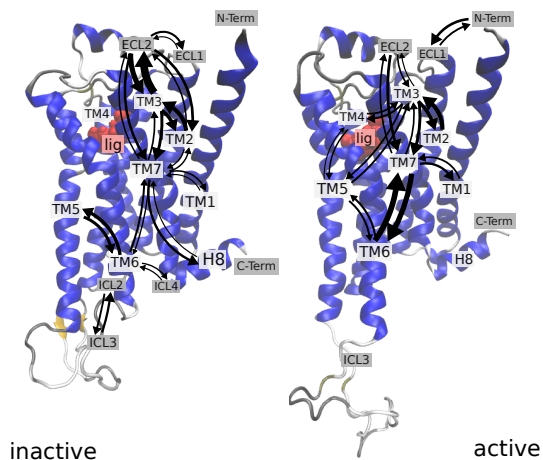


FIG. 7. The secondary structure contact rates of  $\beta_2$ AR visualized in a snapshot of the protein through black arrows with an arrow line width is proportional to the rates.

lices.

Additionally, we calculated the energy transfer within a crystal structure of an active  $\beta_2$ AR bound to adrenaline.<sup>63</sup> The results are presented in Tabs. S5 to S7 and Fig. S2. Although we observe differences in some rates, especially a decrease of the transfer rate between adrenaline and Asp113 by a factor of  $\sim 2$ , the overall time course of energy transfer is very similar to our results with the docked ligand. As the hydrogen bond energy transfer forms the bottleneck step in vibrational energy transport in  $\beta_2$ AR, the overall time course of the transfer is not affected as long as  $D_B \gg D_C$ . This observation supporting our approach to evaluate energy trans-

port within  $\beta_2$ AR based on docking adrenaline into two receptor structures that were not crystallized with this ligand.

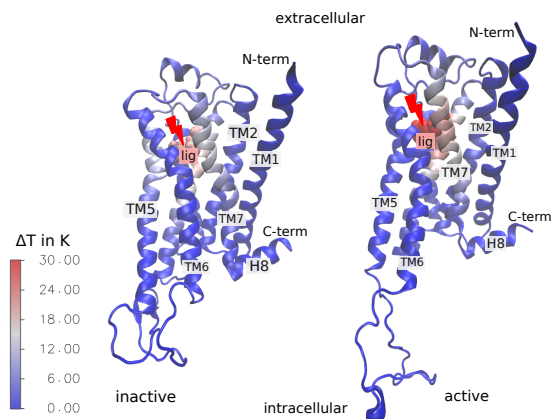


FIG. 8.  $\beta_2$ AR shown 10 ps after heating the ligand. The heated ligand adrenaline is indicated by a red lightning bolt. The coloration shows the local temperatures of residues.

Lastly, to check if a single crystal structure is sufficient to predict the overall energy flow, we compared to energy transport results obtained for a set of snapshots from MD simulations (see Methods). Tables S8 to S10 show that the number of contacts increases by a factor of  $\sim 3$ , i.e., 141 (active) and 158 (inactive receptor) contacts in MD simulations vs. 51 (active) and 66 (inactive receptor) contacts in the crystal structure. As the majority shows only weak couplings, however, the additional contacts do not cause a significant change of the time evolution of the energy distribution (Fig. S3). At least in the case of 7TM proteins, using a single crystal structure seems sufficient to reflect the overall vibrational energy transfer.

## DISCUSSION AND CONCLUSION

We have presented a computational approach that allows us to readily compute the energy transport in any protein. As input we solely need a protein structure, which e.g. can be deduced from crystal structural data. Hence our master equation model may account for potential structural heterogeneity only through an average over various structures. We note that heterogeneous averaging should be appropriate, because of the timescale separation between the fast (ps) energy transport and the slow (ns to ms) conformational dynamics. Moreover, the scaling rules rest on the assumption of a diffusive energy flow, which is expected to be valid for a protein at room temperature.<sup>9</sup> Finally, we have focused on backbone and contacts transport between standard residues, and have not specifically parameterized specific cofactors, such as chromophores. This should be sufficient, when we are interested in the overall energy flow of the protein, which is the goal of this paper. The model needs to be extended, when we want to compare to a specific experiment as in Ref. 10.

We applied the method to three different systems, bR, Rho and  $\beta_2$ AR, all from the group of heptahelical transmembrane proteins. The first two are photoreceptors, which are activated by the absorption of an incoming photon, and are especially interesting to consider as they need to dissipate the energy of the absorbed light quantum. Even though the three systems appear similar in structure, their energy transport mechanisms differ vastly.

bR manages to quickly direct excess energy out of the protein and thus seems well suited to deal with the photon that it absorbs through the retinal. As the two investigated states are very similar in their secondary structure rates, they seem equally well suited for dissipating excess energy out of the protein. The TM7 helix seems to act like a "lightning rod" as it directs the energy out of the protein and into the solvent.

Rho, on the other hand, exhibits a rather poor energy dissipation: excess energy mostly spreads along the backbone within TM7, but does not quickly reach a part of the protein where it could dissipate into a surrounding medium. Moreover, despite still covalently binding the retinal cofactor, the active state seems less suited for quickly distributing energy, which might potentially lead to overheating by additionally absorbed photons. One may speculate that this problem is potentially solved by the hydrolysis of the Schiff base between protein and retinal and its subsequent dissociation.

We finally considered  $\beta_2$ AR, which does not belong to the group of photoreceptive proteins. When heating the ligand, the energy flows into the protein via contacts with the ligand and is thus already much more distributed than in the other systems, where only one entry way into the main bulk of the protein is given. However, from these entry points, the energy does not reach far and is consequently not dissipated much in the protein. Because there is no photoexcitation present in this protein, and adrenaline binding introduces a negligible amount of energy into the protein, however, there is also no need for an evolutionary adaption for the protein for optimal energy dissipation.

Another reason to consider the energy flow in  $\beta_2$ AR is that its energy transport pathways are believed to be linked to channels of allosteric communication.<sup>35</sup> Allostery may be mediated by structural and dynamical changes of a protein,<sup>18</sup> and we indeed observed structural differences between the inactive and active state of  $\beta_2$ AR. These conformational changes are typically associated with changes of interresidue contacts, which stabilize the two states. Since the energy transport in a protein is also mediated by interresidue contacts, various authors have studied potential interrelations of the two processes.<sup>11–17</sup> While it seems appealing to rationalize elusive allosteric transitions via simple visualizations of vibrational energy transport (as, e.g., shown in Figs. 3, 5 and 8), there are several limitations to this analogy.

First off, it should be stressed that energy transport and allostery constitute different physical processes. En-

ergy transport reflects the instantaneous mechanical connectivity of the protein, and occurs therefore on a picosecond timescale. Allostery, on the other hand, is believed to reflect structural changes<sup>97</sup> (e.g., changes of interresidue contacts or side chain dihedral angles) which typically take place on a micro- or millisecond timescale.<sup>98–100</sup> Secondly, our scaling rule for contact transport [Eq. (3)] provides a direct relation between protein energy flow and polar contacts. Within this approximation, the contact energy transport only gives information about the contacts that is already known from the protein structure. Finally, nonpolar contacts are negligible for energy transport,<sup>44,51</sup> but are clearly important for allostery. In the case of  $\beta_2$ AR, for example, Fleetwood et al.<sup>101</sup> recently established the importance of hydrophobic contacts forming microswitches. While the energy flow may highlight aspects of the interresidue couplings of a protein, it therefore seems not particularly suited to explain allosteric phenomena.

#### Supplementary Information

Ten Supplementary Tables detailing on energy transfer rates and three Supplementary Figures displaying the energy distribution in protein over time.

#### Acknowledgments

The authors thank Luis Valino-Borau for helpful discussions. This work has been supported by the Deutsche Forschungsgemeinschaft (DFG) via project STO247/10 and the Research Unit FOR 5099 "Reducing complexity of nonequilibrium" (project No. 431945604).

<sup>1</sup>D. M. Leitner and J. E. Straub, *Proteins: Energy, Heat and Signal Flow*, Taylor and Francis/CRC Press, London, 2009.

<sup>2</sup>C. Riedel, R. Gabizon, C. A. M. Wilson, K. Hamadani, K. Tsekouras, S. Marqusee, S. Pressé, and C. Bustamante, The heat released during catalytic turnover enhances the diffusion of an enzyme, *Nature* **517**, 227 (2015).

<sup>3</sup>P. M. Champion, Following the flow of energy in biomolecules, *Science* **310**, 980 (2005).

<sup>4</sup>W. Domcke and G. Stock, Theory of ultrafast nonadiabatic excited-state processes and their spectroscopic detection in real time, *Adv. Chem. Phys.* **100**, 1 (1997).

<sup>5</sup>Y. Mizutani and T. Kitagawa, Direct observation of cooling of heme upon photodissociation of carbonmonoxy myoglobin, *Science* **278**, 443 (1997).

<sup>6</sup>J. Deak, Y. Pang, T. Sechler, Z. Wang, and D. Dlott, Vibrational energy transfer across a reverse micelle surfactant layer, *Science* **306**, 473 (2004).

<sup>7</sup>V. Botan, E. Backus, R. Pfister, A. Moretto, M. Crisma, C. Toniolo, P. H. Nguyen, G. Stock, and P. Hamm, Energy transport in peptide helices, *Proc. Natl. Acad. Sci. USA* **104**, 12749 (2007).

<sup>8</sup>G. Li, D. Magana, and R. B. Dyer, Anisotropic energy flow and allosteric ligand binding in albumin, *Nat. Commun.* **5**, 3100 (2014).

<sup>9</sup>I. V. Rubtsov and A. L. Burin, Perspective: Ballistic and diffusive vibrational energy transport in molecules, *J. Chem. Phys.* **150**, 020901 (2019).

<sup>10</sup>E. Deniz et al., Through bonds or contacts? mapping protein vibrational energy transfer using non-canonical amino acids., *Nat. Commun.* **12**, 3284 (2021).

<sup>11</sup>N. Ota and D. A. Agard, Intramolecular signaling pathways revealed by molecular anisotropic thermal diffusion, *J. Mol. Biol.* **351**, 345 (2005).

<sup>12</sup>T. Ishikura and T. Yamato, Energy transfer pathways relevant for long-range intramolecular signaling of photosensory protein



- revealed by microscopic energy conductivity analysis, *Chem. Phys. Lett.* **432**, 533 (2006).
- <sup>13</sup>P. H. Nguyen, P. Derreumaux, and G. Stock, Energy flow and long-range correlations in guanine-binding riboswitch: A nonequilibrium molecular dynamics study, *J. Phys. Chem. B* **113**, 9340 (2009).
  - <sup>14</sup>L. Martinez, A. C. M. Figueira, P. Webb, I. Polikarpov, and M. S. Skaf, Mapping the intramolecular vibrational energy flow in proteins reveals functionally important residues, *J. Phys. Chem. Lett.* **2**, 2073 (2011).
  - <sup>15</sup>A. S. T. Ribeiro and V. Ortiz, Energy propagation and network energetic coupling in proteins, *J. Phys. Chem. B* **119**, 1835 (2015).
  - <sup>16</sup>J. K. Weber, D. Shukla, and V. S. Pande, Heat dissipation guides activation in signaling proteins, *Proc. Natl. Acad. Sci. USA* **112**, 10377 (2015).
  - <sup>17</sup>L. Maggi, P. Carloni, and G. Rossetti, Vibrational energy in proteins correlates with topology, *J. Phys. Chem. Lett.* **9**, 6393 (2018).
  - <sup>18</sup>S. J. Wodak et al., Allostery in its many disguises: From theory to applications, *Structure* **27**, 566 (2019).
  - <sup>19</sup>W. R. Briggs and J. L. Spudich, *Handbook of photosensory receptors*, Vch Verlagsgesellschaft MbH, 2005.
  - <sup>20</sup>O. P. Ernst, D. T. Lodowski, M. Elstner, P. Hegemann, L. S. Brown, and H. Kandori, Microbial and animal rhodopsins: Structures, functions, and molecular mechanisms, *Chem. Rev.* **114**, 126 (2022).
  - <sup>21</sup>A. Rozenberg, K. Inoue, H. Kandori, and O. B ej a, Microbial Rhodopsins: The Last Two Decades., *Annu. Rev. Microbiol.* **75**, 427 (2021).
  - <sup>22</sup>S. O. Smith, Structure and activation of the visual pigment rhodopsin., *Annu. Rev. Biophys.* **39**, 309 (2010).
  - <sup>23</sup>J. K. Lanyi, Bacteriorhodopsin, *Annu. Rev. Physiol.* **66**, 665 (2004).
  - <sup>24</sup>D. Oesterhelt and W. Stoekenius, Rhodopsin-like protein from the purple membrane of halobacterium halobium, *Nat. New Biol.* **233**, 149 (1971).
  - <sup>25</sup>D. Oesterhelt and W. Stoekenius, Functions of a new photoreceptor membrane, *Proc. Natl. Acad. Sci. USA* **70**, 2853 (1973).
  - <sup>26</sup>R. Fredriksson, M. C. Lagerstrom, L. G. Lundin, and H. B. Schioth, The G-protein-coupled receptors in the human genome form five main families. Phylogenetic analysis, paralog groups, and fingerprints, *Mol. Pharmacol.* **63**, 1256 (2003).
  - <sup>27</sup>R. J. Lefkowitz, Historical review: a brief history and personal retrospective of seven-transmembrane receptors., *Trends Pharmacol. Sci.* **25**, 413 (2004).
  - <sup>28</sup>A. J. Venkatakrishnan, X. Deupi, G. Lebon, C. G. Tate, G. F. Schertler, and M. M. Babu, Molecular signatures of G-protein-coupled receptors, *Nature* **494**, 185 (2013).
  - <sup>29</sup>S. Wolf and S. Gr unewald, Sequence, Structure and Ligand Binding Evolution of Rhodopsin-Like G Protein-Coupled Receptors: A Crystal Structure-Based Phylogenetic Analysis, *Plos One* **10**, e0123533 (2015).
  - <sup>30</sup>S. O. Smith, J. Lugtenburg, and R. Mathies, Determination of Retinal Chromophore Structure in Bacteriorhodopsin with Resonance Raman-Spectroscopy, *J. Membr. Biol.* **85**, 95 (1985).
  - <sup>31</sup>S. Mous et al., Dynamics and mechanism of a light-driven chloride pump, *Science* (2022).
  - <sup>32</sup>R. Piechnick, E. Ritter, P. W. Hildebrand, O. P. Ernst, P. Scheerer, K. P. Hofmann, and M. Heck, Effect of channel mutations on the uptake and release of the retinal ligand in opsin, *Proc. Natl. Acad. Sci. USA* **109**, 5247 (2012).
  - <sup>33</sup>P. D. Kiser, M. Golczak, and K. Palczewski, Chemistry of the retinoid (visual) cycle., *Chem. Rev.* **114**, 194 (2014).
  - <sup>34</sup>B. K. Kobilka, Structural insights into adrenergic receptor function and pharmacology, *Trends Pharmacol. Sci.* **32**, 213 (2011).
  - <sup>35</sup>H. Poudel and D. M. Leitner, Activation-induced reorganization of energy transport networks in the  $\beta_2$  adrenergic receptor, *J. Phys. Chem. B* **125**, 6522 (2021).
  - <sup>36</sup>P. H. Nguyen and G. Stock, Nonequilibrium molecular-dynamics study of the vibrational energy relaxation of peptides in water, *J. Chem. Phys.* **119**, 11350 (2003).
  - <sup>37</sup>H. Fujisaki and J. E. Straub, Vibrational energy relaxation in proteins, *Proc. Natl. Acad. Sci. USA* **102**, 6726 (2005).
  - <sup>38</sup>S. M. Park, P. H. Nguyen, and G. Stock, Molecular dynamics simulation of cooling: Heat transfer from a photoexcited peptide to the solvent, *J. Chem. Phys.* **131**, 184503 (2009).
  - <sup>39</sup>P. H. Nguyen, S. M. Park, and G. Stock, Nonequilibrium molecular dynamics simulation of the energy transport through a peptide helix, *J. Chem. Phys.* **132**, 025102 (2010).
  - <sup>40</sup>M. A. Soler, A. Bastida, M. H. Farag, J. Zuniga, and A. Requena, A method for analyzing the vibrational energy flow in biomolecules in solution, *J. Chem. Phys.* **135**, 204106 (2011).
  - <sup>41</sup>W. B. Wang, Y. Liang, J. Zhang, Y. D. Wu, J. J. Du, Q. M. Li, J. Z. Zhu, and J. G. Su, Energy transport pathway in proteins: Insights from non-equilibrium molecular dynamics with elastic network model, *Sci. Rep.* **8**, 9487 (2018).
  - <sup>42</sup>J. E. Elenewski, K. A. Velizhanin, and M. Zwolak, Topology, landscapes, and biomolecular energy transport, *Nat. Commun.* **10**, 4662 (2019).
  - <sup>43</sup>A. Gulzar, L. Vali no Borau, S. Buchenberg, S. Wolf, and G. Stock, Energy transport pathways in proteins: A nonequilibrium molecular dynamics simulation study, *J. Chem. Theory Comput.* **15**, 5750 (2019).
  - <sup>44</sup>H. Poudel, K. M. Reid, T. Yamato, and D. M. Leitner, Energy transfer across nonpolar and polar contacts in proteins: Role of contact fluctuations, *J. Phys. Chem.* **124B**, 9852 (2020).
  - <sup>45</sup>X. Yu and D. Leitner, Vibrational energy transfer and heat conduction in a protein, *J. Phys. Chem. B* **107**, 1698 (2003).
  - <sup>46</sup>D. M. Leitner, Frequency-resolved communication maps for proteins and other nanoscale materials, *J. Chem. Phys.* **130**, 195101 (2009).
  - <sup>47</sup>Y. Kong and M. Karplus, Signaling pathways of PDZ2 domain: A molecular dynamics interaction correlation analysis, *Proteins* **74**, 145 (2009).
  - <sup>48</sup>A. S. T. Ribeiro and V. Ortiz, Determination of signaling pathways in proteins through network theory: Importance of the topology, *J. Comput. Chem.* **10**, 1762 (2014).
  - <sup>49</sup>D. M. Leitner, S. Buchenberg, P. Brettl, and G. Stock, Vibrational energy flow in the villin headpiece subdomain: Master equation simulations, *J. Chem. Phys.* **142**, 075101 (2015).
  - <sup>50</sup>T. Ishikura, Y. Iwata, T. Hatano, and T. Yamato, Energy exchange network of inter-residue interactions within a thermally fluctuating protein molecule: A computational study, *J. Comput. Chem.* **36**, 1709 (2015).
  - <sup>51</sup>S. Buchenberg, D. M. Leitner, and G. Stock, Scaling rules for vibrational energy transport in globular proteins, *J. Phys. Chem. Lett.* **7**, 25 (2016).
  - <sup>52</sup>K. Reid, T. Yamato, and D. M. Leitner, Scaling of rates of vibrational energy transfer in proteins with equilibrium dynamics and entropy, *J. Phys. Chem. B* **122**, 9331 (2018).
  - <sup>53</sup>L. Vali no Borau, A. Gulzar, and G. Stock, Master equation model to predict energy transport pathways in proteins, *J. Chem. Phys.* **152**, 045103 (2020).
  - <sup>54</sup>T. Okada, M. Sugihara, A.-N. Bondar, M. Elstner, P. Entel, and V. Buss, The Retinal Conformation and its Environment in Rhodopsin in Light of a New 2.2  Crystal Structure, *J. Mol. Biol.* **342**, 571 (2004).
  - <sup>55</sup>V. Cherezov et al., High-Resolution Crystal Structure of an Engineered Human 2-Adrenergic G Protein Coupled Receptor, *Science* **318**, 1258 (2007).
  - <sup>56</sup>H.-W. Choe, Y. J. Kim, J. H. Park, T. Morizumi, E. F. Pai, N. Krau , K. P. Hofmann, P. Scheerer, and O. P. Ernst, Crystal structure of metarhodopsin II, *Nature* **471**, 651 (2011).
  - <sup>57</sup>S. G. Rasmussen, H. J. Choi, J. J. Fung, and E. Pardon, Structure of a nanobody-stabilized active state of the  $\beta_2$  adrenoceptor, *Nature* **469**, 175 (2011).
  - <sup>58</sup>E. Nango et al., A three-dimensional movie of structural changes in bacteriorhodopsin, *Science* **354**, 1552 (2016).

- <sup>59</sup>T. Weinert et al., Proton uptake mechanism in bacteriorhodopsin captured by serial synchrotron crystallography, *Science* **365**, 61 (2019).
- <sup>60</sup>S. Egorov, K. Everitt, and J. Skinner, Quantum dynamics and vibrational relaxation, *J. Phys. Chem. A* **103**, 9494 (1999).
- <sup>61</sup>M. Schade and P. Hamm, Vibrational energy transport in the presence of intrasite vibrational energy redistribution, *J. Chem. Phys.* **131**, 044511 (2009).
- <sup>62</sup>G. Stock, Classical simulation of quantum energy flow in biomolecules, *Phys. Rev. Lett.* **102**, 118301 (2009).
- <sup>63</sup>A. M. Ring, A. Manglik, A. C. Kruse, M. D. Enos, W. I. Weis, K. C. Garcia, and B. K. Kobilka, Adrenaline-activated structure of  $\beta$ 2-adrenoceptor stabilized by an engineered nanobody., *Nature* **502**, 575 (2013).
- <sup>64</sup>M. H. Olsson, C. R. S ndergaard, M. Rostkowski, and J. H. Jensen, PROPKA3: consistent treatment of internal and surface residues in empirical p K a predictions, *J. Chem. Theory Comput.* **7**, 525 (2011).
- <sup>65</sup>C. R. S ndergaard, M. H. M. Olsson, M. Rostkowski, and J. H. Jensen, Improved Treatment of Ligands and Coupling Effects in Empirical Calculation and Rationalization of pKa Values., *J. Chem. Theory Comput.* **7**, 2284 (2011).
- <sup>66</sup>T. J. Dolinsky, J. E. Nielsen, J. A. McCammon, and N. A. Baker, PDB2PQR: an automated pipeline for the setup of Poisson-Boltzmann electrostatics calculations., *Nucl. Acids Res.* **32**, W665 (2004).
- <sup>67</sup>E. Jurrus et al., Improvements to the APBS biomolecular solvation software suite., *Protein Sci.* **27**, 112 (2018).
- <sup>68</sup>A. Waterhouse et al., SWISS-MODEL: homology modelling of protein structures and complexes., *Nucl. Acids Res.* **46**, W296 (2018).
- <sup>69</sup>O. Trott and A. J. Olson, AutoDock Vina: improving the speed and accuracy of docking with a new scoring function, efficient optimization, and multithreading., *J. Comput. Chem.* **31**, 455 (2010).
- <sup>70</sup>Richard J. Gowers et al., MDAnalysis: A Python Package for the Rapid Analysis of Molecular Dynamics Simulations, in *Proceedings of the 15th Python in Science Conference*, edited by Sebastian Benthal and Scott Rostrup, pages 98 – 105, 2016.
- <sup>71</sup>N. Michaud-Agrawal, E. J. Denning, T. B. Woolf, and O. Beckstein, Mdanalysis: A toolkit for the analysis of molecular dynamics simulations, *J. Comput. Chem.* **32**, 2319 (2011).
- <sup>72</sup>T. H. Schmidt and C. Kandt, LAMBADA and InflateGRO2: efficient membrane alignment and insertion of membrane proteins for molecular dynamics simulations., *J. Chem. Inf. Model.* **52**, 2657 (2012).
- <sup>73</sup>V. Hornak, R. Abel, A. Okur, B. Strockbine, A. Roitberg, and C. Simmerling, Comparison of multiple Amber force fields and development of improved protein backbone parameters, *Proteins* **65**, 712 (2006).
- <sup>74</sup>R. B. Best and G. Hummer, Optimized molecular dynamics force fields applied to the helix-coil transition of polypeptides, *J. Phys. Chem. B* **113**, 9004 (2009).
- <sup>75</sup>O. Berger, O. Edholm, and F. J hning, Molecular dynamics simulations of a fluid bilayer of dipalmitoylphosphatidylcholine at full hydration, constant pressure, and constant temperature, *Biophys. J.* **72**, 2002 (1997).
- <sup>76</sup>A. Cordonm , G. Caltabiano, and L. Pardo, Membrane Protein Simulations Using AMBER Force Field and Berger Lipid Parameters, *J. Chem. Theory Comput.* **8**, 948 (2012).
- <sup>77</sup>W. L. Jorgensen, J. Chandrasekhar, J. D. Madura, R. W. Impey, and M. Klein, Comparison of simple potential functions for simulating liquid water, *J. Chem. Phys.* **79**, 926 (1983).
- <sup>78</sup>J. Wang and R. Br schweiler, 2D entropy of discrete molecular ensembles, *J. Chem. Theory Comput.* **2**, 18 (2006).
- <sup>79</sup>A. W. Sousa da Silva and W. F. Vranken, ACPYPE - AnteChamber PYthon Parser interfacE, *BMC Res. Notes* **5**, 367 (2012).
- <sup>80</sup>J. M. Wang, R. M. Wolf, J. W. Caldwell, P. A. Kollman, and D. A. Case, Development and testing of a general amber force field, *J. Comput. Chem.* **25**, 1157 (2004).
- <sup>81</sup>A. Jakalian, B. L. Bush, D. B. Jack, and C. I. Bayly, Fast, efficient generation of high-quality atomic Charges. AM1-BCC model: I. Method, *J. Comput. Chem.* **21**, 132 (2000).
- <sup>82</sup>A. Jakalian, D. B. Jack, and C. I. Bayly, Fast, efficient generation of high-quality atomic charges. AM1-BCC model - II. Parameterization and validation., *J. Comput. Chem.* **23**, 1623 (2002).
- <sup>83</sup>M. J. Abraham, T. Murtola, R. Schulz, S. Pall, J. C. Smith, B. Hess, and E. Lindahl, Gromacs: High performance molecular simulations through multi-level parallelism from laptops to supercomputers, *SoftwareX* **1**, 19 (2015).
- <sup>84</sup>T. Darden, D. York, and L. Petersen, Particle mesh Ewald: An  $N \log(N)$  method for Ewald sums in large systems, *J. Chem. Phys.* **98**, 10089 (1993).
- <sup>85</sup>B. Hess, H. Bekker, H. J. C. Berendsen, and J. G. E. M. Fraaije, LINCS: A linear constraint solver for molecular simulations, *J. Comp. Chem.* **18**, 1463 (1997).
- <sup>86</sup>S. Nos , A unified formulation of the constant temperature molecular dynamics methods, *J. Chem. Phys.* **81**, 511 (1984).
- <sup>87</sup>W. G. Hoover, Canonical dynamics: Equilibrium phase-space distributions, *Phys. Rev. A* **31**, 1695 (1985).
- <sup>88</sup>H. J. C. Berendsen, J. P. M. Postma, W. F. van Gunsteren, A. Dinola, and J. R. Haak, Molecular dynamics with coupling to an external bath, *J. Chem. Phys.* **81**, 3684 (1984).
- <sup>89</sup>M. Parrinello and A. Rahman, Polymorphic transitions in single crystals: A new molecular dynamics method, *J. Appl. Phys.* **52**, 7182 (1981).
- <sup>90</sup>W. Humphrey, A. Dalke, and K. Schulten, VMD – Visual Molecular Dynamics, *J. Mol. Graph.* **14**, 33 (1996).
- <sup>91</sup>B. A. Wallace and N. Kohl, The C-Terminus of Bacteriorhodopsin Is a Random Coil, *Biochimica et Biophysica Acta* **777**, 93 (1984).
- <sup>92</sup>M. J. Liao and H. Khorana, Removal of the carboxyl-terminal peptide does not affect refolding or function of bacteriorhodopsin as a light-dependent proton pump., *Biophys. J.* **259**, 4194 (1984).
- <sup>93</sup>G. J. Turner, S. Chittiboyina, L. Pohren, K. G. Hines, J. J. Correia, and D. C. Mitchell, The bacteriorhodopsin carboxyl-terminus contributes to proton recruitment and protein stability., *Biochemistry* **48**, 1112 (2009).
- <sup>94</sup>J. Kim, C. Altenbach, M. Kono, D. Oprian, W. Hubbell, and H. Khorana, Structural origins of constitutive activation in rhodopsin: Role of the K296/E113 salt bridge, *Proc. Natl. Acad. Sci. USA* **101**, 12508 (2004).
- <sup>95</sup>C.-J. Tsai et al., Cryo-EM structure of the rhodopsin-Gai- $\beta$ - $\gamma$  complex reveals binding of the rhodopsin C-terminal tail to the  $g\beta$  subunit., *eLife* **8** (2019).
- <sup>96</sup>K. Gerwert, E. Freier, and S. Wolf, The role of protein-bound water molecules in microbial rhodopsins, *BBA - Bioenergetics* **1837**, 606 (2014).
- <sup>97</sup>R. Nussinov and C.-J. Tsai, Allostery without a conformational change? Revisiting the paradigm, *Curr. Opin. Struc. Biol.* **30**, 17 (2015).
- <sup>98</sup>S. Br schweiler, P. Schanda, K. Kloiber, B. Brutscher, G. Kontaxis, R. Konrat, and M. Tollinger, Direct observation of the dynamic process underlying allosteric signal transmission, *J. Am. Chem. Soc.* **131**, 3063 (2009).
- <sup>99</sup>B. Buchli, S. A. Waldauer, R. Walser, M. L. Donten, R. Pfister, N. Bloechliger, S. Steiner, A. Caffisch, O. Zerbe, and P. Hamm, Kinetic response of a photoperturbed allosteric protein, *Proc. Natl. Acad. Sci. USA* **110**, 11725 (2013).
- <sup>100</sup>O. Bozovic, C. Zanobini, A. Gulzar, B. Jankovic, D. Buhrike, M. Post, S. Wolf, G. Stock, and P. Hamm, Real-time observation of ligand-induced allosteric transitions in a PDZ domain, *Proc. Natl. Acad. Sci. USA* **117**, 26031 (2020).
- <sup>101</sup>O. Fleetwood, J. Carlsson, and L. Delemotte, Identification of ligand-specific g protein-coupled receptor states and prediction of downstream efficacy via data-driven modeling, *eLife* **10**, e60715 (2021).

# Supporting Information: Energy Transport and its Function in heptahelical Proteins

Nadja Helmer, Steffen Wolf, and Gerhard Stock  
*Biomolecular Dynamics, Institute of Physics, Albert Ludwigs University, 79104 Freiburg, Germany.*  
(Dated: October 14, 2022)

## I. SUPPLEMENTARY TABLES

Table S1. Contact between the different residues for the inactive and active state of bacteriorhodopsin. The rates are given in  $\text{ps}^{-1}$ . According to convention, the residues start at ID 5.

Residues		Rates	
Res 1	Res 2	Inactive	Active
Arg7	Met60	0.13	0.11
Arg7	Leu61	0.14	
Glu9	Tyr79	0.26	0.16
Leu13	Thr17	0.17	0.17
Met20	Thr24	0.15	0.18
Asp36	Gly231	0.09	
Phe42	Thr46		0.15
Thr46	Asp96	0.16	
Tyr57	Asp212	0.16	0.15
Ser59	Tyr64		0.26
Ser59	Gly65	0.10	0.09
Gly65	Ala81	0.14	0.10
Thr67	Ile78	0.40	0.35
Val69	Asn76	0.28	0.11
Phe71	Asn76	0.08	
Asp85	Thr89		0.20
Trp86	Thr90	0.14	0.18
Trp86	Asp212		0.11
Ala98	Ala103	0.16	0.12
Asp102	Lys159	0.21	
Ile117	Thr121	0.15	0.16
Met118	Ser141	0.14	0.13
Val124	Thr128	0.19	0.21
Ala126	Arg134	0.20	0.21
Thr128	Arg134	0.21	0.18
Arg134	Glu194	0.24	0.17
Trp138	Thr142	0.11	0.12
Trp138	Pro186	0.12	0.08
Arg164	Phe230	0.25	
Pro165	Ser169	0.17	0.14
Glu166	Thr170	0.16	
Leu174	Thr178		0.15
Val179	Ser183	0.14	0.15
Tyr185	Asp212	0.15	0.10
Leu190	Ala196	0.14	0.14
Ile191	Val199	0.14	0.15
Gly192	Gly197	0.15	
Ser193	Glu204	0.44	0.35
Leu201	Thr205	0.15	0.09
Val210	Ser214		0.16

Table S2. Contact rates between the different residues for the inactive and active state of rhodopsin. The rates are given in  $\text{ps}^{-1}$ . The residue IDs start at 1.

Residues		Rates	
Res 1	Res 2	Inactive	Active
Met1	Ser14	0.08	
Asn2	Gly280	0.16	
Thr4	Val11	0.42	0.16
Thr4	Phe13	0.25	0.26
Pro7	Arg177	0.21	
Asn15	Val20	0.20	
Arg21	Gln28	0.16	0.12
Ser22	Ala26	0.13	0.12
Pro23	Phe103	0.20	
Gln28	Gly101		0.11
Tyr29	His100	0.11	0.10
Pro34	Ser38	0.11	0.11
Tyr43	Phe293	0.22	
Gly51	Asn55	0.27	0.30
Ile54	Thr58	0.19	0.16
Asn55	Asp83	0.16	0.25
Asn55	Ala299	0.18	0.15
Thr58	Thr62	0.21	0.16
Tyr60	Gln64		0.08
Val61	His65		0.17
Thr62	Arg69	0.21	
Val63	Arg69	0.19	0.23
Leu68	Asn73		0.19
Asn78	Trp161	0.22	0.13
Val87	Thr92		0.08
Phe88	Thr92	0.20	
Gly89	Thr93		0.28
Gly90	Thr94		0.24
Thr93	Thr97	0.19	
Thr94	Ser98	0.16	0.19
Tyr96	His100		0.15
Thr97	Tyr102		0.11
Thr97	Cys185		0.27
Glu113	Cys187	0.14	0.15
Glu113	Lys296	0.11	
Gly114	Thr118	0.28	0.35
Glu122	His211	0.15	

Residues		Rates	
Res 1	Res 2	Inactive	Active
Ile123	Ser127		0.15
Arg135	Glu247	0.18	
Met163	His211		0.13
Ala166	Tyr206	0.35	0.36
Ala168	Tyr178	0.31	0.35
Pro170	Trp175	0.15	
Gly174	Thr198	0.22	
Ser176	Thr198	0.24	0.19
Arg177	Asp190	0.23	0.36
Ile179	Gly188	0.21	0.17
Glu181	Ser186	0.15	0.20
Glu181	Tyr268	0.17	0.14
Thr193	Asn200	0.10	0.18
His195	Asn200	0.09	0.09
Gln225	Thr229	0.16	
Lys231	Glu247		0.21
Ala234	Gln244		0.18
Ala235	Glu239	0.24	
Ser240	Gln244		0.16
Glu247	Thr251	0.16	0.16
Glu249	Lys311	0.10	
Phe273	Thr277		0.12
Tyr274	His278	0.13	
Gly284	Met288		0.20
Pro285	Thr289	0.22	0.17
Phe293	Thr297		0.16
Phe294	Tyr301		0.17
Thr297	Tyr301	0.18	
Ile307	Arg314	0.17	
Met308	Arg314		0.15
Met309	Arg314		0.10
Lys311	Asn315	0.18	
Gln312	Thr335	0.10	
Asn315	Thr319		0.13
Cys316	Thr320	0.28	0.16
Ser338	Ser343	0.36	

Table S3. Rates of Rhodopsin with surrounding water molecules. In the inactive state, we find 37 contacts with water (yielding 28 contact rates). In the active state we only identify 17 water contacts (16 contact rates). The rates are given in  $\text{ps}^{-1}$ .

Residues		Rates		Residues		Rates	
Res 1	Res 2	Inactive	Active	Res 1	Res 2	Inactive	Active
Gly3	Water	0.16	0.16	Cys185	Water		0.06
Glu5	Water		0.09	Cys187	Water	0.07	
Asn8	Water	0.08		Tyr191	Water	0.04	
Tyr10	Water	0.11		Tyr192	Water	0.08	
Pro12	Water	0.08		Thr193	Water	0.07	
Ser14	Water	0.09	0.15	Glu196	Water	0.10	
Pro34	Water		0.11	Thr229	Water		0.10
Gln64	Water		0.06	Gln236	Water		0.07
Asn73	Water	0.10		Glu239	Water		0.09
Gly89	Water	0.20		Glu249	Water	0.05	
Ser98	Water		0.11	Met257	Water	0.09	0.12
Glu113	Water	0.08		Ala260	Water		0.10
Gly120	Water	0.07		Cys264	Water	0.12	
Ala153	Water		0.12	Gly284	Water	0.27	
Pro171	Water	0.11		Pro291	Water	0.08	
Ser176	Water	0.11		Ser298	Water	0.23	0.07
Tyr178	Water	0.15		Asn302	Water	0.08	
Pro180	Water	0.14		Cys323	Water		0.05
Glu181	Water	0.15	0.15	Asp331	Water	0.04	
				Glu332	Water	0.11	

Table S4. Contact rates for the inactive and active state of  $\beta_2$ AR. The rates are given in  $\text{ps}^{-1}$ . According to convention, the residue IDs start at 29.

Residues		Rates		Residues		Rates	
Res 1	Res 2	Inactive	Active	Res 1	Res 2	Inactive	Active
Glu30	Lys97		0.25	Ala176	Phe194		0.18
Gly37	Ser41	0.24	0.27	Gln179	Asn183		0.14
Ile47	Asn51	0.13	0.18	Tyr185	Phe194		0.13
Asn51	Ser319	0.11	0.17	Asp192	Lys305	0.24	0.26
Val52	Thr56	0.21	0.24	Tyr199	Ser203		0.15
Ala57	Phe61		0.25	Ala200	Ser204	0.17	0.18
Ala59	Gln65	0.21		Ser203	Adr343	0.29	
Leu64	Asn69	0.17	0.16	Tyr209	Phe290	0.14	0.19
Thr68	Asp130	0.21		Val216	Ser220		0.21
Asn69	Thr73	0.11	0.15	Tyr219	Leu272	0.15	
Asp79	Ser120		0.16	Arg221	Glu225		0.18
Asp79	Ser319	0.12		Glu225	Gln229		0.18
Val86	Trp109	0.19	0.24	Arg228	Glu249	0.34	
His93	Cys191	0.15		Gln231	Glu268		0.09
Trp99	Thr189	0.11		Asp234	Arg239	0.52	
Asn103	Ala186		0.11	Asp234	Arg260	0.55	
Cys106	Thr110	0.23	0.24	Ser236	Asp251		0.48
Glu107	Ser111	0.18	0.19	Gly238	Asn244		0.21
Glu107	Gln170		0.19	Arg239	His256	0.13	
Glu107	Tyr174	0.30		Phe240	Thr254	0.18	
Glu107	Arg175	0.41		His241	Gly252	0.10	
Asp113	Tyr316	0.18	0.28	Val242	Gln250	0.17	
Asp113	Adr343	0.71	0.57	Gln243	Glu249	0.13	
Val114	Thr118	0.19	0.17	Asn244	Val248	0.18	
Cys116	Ser120	0.23		Glu249	Arg253		0.43
Ala119	Thr123	0.26	0.17	Lys270	Thr274		0.15
Glu122	Val206		0.17	Lys270	Arg328	0.13	
Asp130	Ser143	0.21		Ile277	Thr281	0.20	0.15
Arg131	Tyr141	0.15		Ile278	Tyr326		0.24
Arg131	Gln142	0.16		Met279	Thr283	0.22	0.20
Tyr132	Thr136	0.12	0.13	Trp286	Asn318		0.09
Ala134	Tyr141	0.17		Phe289	Asn293	0.16	
Lys140	Gln243	0.18		Asn293	Tyr308	0.19	0.22
Lys147	Arg151	0.17		Val295	Gln299		0.14
Val157	Ser161	0.16	0.20	His296	Asn301	0.12	
Val160	Thr164		0.20	His296	Ile303	0.09	
Ser161	Ser165	0.20	0.21	Asn312	Adr343	0.27	0.27
Thr164	Tyr199		0.14	Gly315	Ser319	0.11	
Pro168	Tyr174	0.20		Tyr316	Gly320	0.08	
Trp173	Asn196		0.16	Asn318	Asn322	0.15	0.22
Tyr174	Asn196	0.10		Cys327	Arg333	0.23	
Arg175	Asn196	0.14	0.12	Arg328	Arg333		0.20
Ala176	Tyr185	0.34		Gln337	Leu342	0.17	

Table S5. Rates of the contacts formed between the ligand adrenaline and  $\beta_2$ AR for the 4LDO state and the 3POG state. The rates are given in  $\text{ps}^{-1}$ .

Residues		Rates	
Res 1	Res 2	4LDO	3POG
Adr	Asp113	0.11	0.27
Adr	Asn312	0.13	0.14

Table S6. Secondary structure rates for both active states, 4LDO (left) and 3P0G (right). The rates are given in  $\text{ps}^{-1}$ .

Sec. Struct.		Rates	
Sec 1	Sec 2	4LDO	3P0G
N-Term	ECL1		0.25
TM1	TM7	0.11	0.17
ICL1	H8	0.09	
TM2	TM3	0.49	0.40
TM3	TM4		0.19
TM3	ECL2	1.03	0.11
TM3	TM5	0.19	0.17
TM3	TM7	0.24	0.28
TM4	TM5	0.21	0.14
ECL2	TM7		0.26
TM5	TM6	0.12	0.19
TM6	TM7	0.29	0.54

Table S7. Contact rates for 4LDO active state of  $\beta_2\text{AR}$ . The rates are given in  $\text{ps}^{-1}$ . According to convention, the residue IDs start at 29.

Residues		Rates		Residues		Rates	
Res 1	Res 2	4LDO	3P0G	Res 1	Res 2	4LDO	3P0G
Glu30	Lys97		0.25	Tyr174	Asn196	0.09	
Gly37	Ser41	0.16	0.27	Arg175	Asn196	0.14	0.12
Ile47	Asn51	0.15	0.18	Ala176	Phe194		0.18
Asn51	Ser319	0.11	0.17	Gln179	Asn183	0.17	0.14
Val52	Thr56	0.15	0.24	Tyr185	Phe194		0.13
Ala57	Phe61		0.25	Asp192	Lys305		0.26
Arg63	Asp331	0.09		Tyr199	Ser203		0.15
Leu64	Asn69	0.15	0.16	Ala200	Ser204		0.18
Thr68	Asp130	0.12		Ser203	Ser207	0.19	
Asn69	Thr73	0.15	0.15	Tyr209	Phe290	0.12	0.19
Asp79	Ser120	0.14	0.16	Val216	Ser220		0.21
Val86	Trp109	0.23	0.24	Arg221	Glu225	0.07	0.18
Ala92	Met96	0.23		Glu225	Gln229	0.22	0.18
Asn103	Ala186		0.11	Gln231	Lys235	0.19	
Asn103	Gln187	0.16		Gln231	Glu268		0.09
Asn103	Glu188	0.22		Asp234	Arg239	0.31	
Cys106	Thr110	0.17	0.24	Lys235	Ser262	0.08	
Glu107	Ser111	0.12	0.19	Ser236	Asp251		0.48
Glu107	Gln170		0.19	Glu237	Arg253	0.20	
Glu107	Tyr174	0.23		Gly238	Asn244		0.21
Glu107	Arg175	0.42		Glu249	Arg253		0.43
Asp113	Tyr316	0.24	0.28	Gly255	Ser262	0.17	
Asp113	Adr343	0.22	0.57	Leu258	Ser262	0.07	
Val114	Thr118	0.18	0.17	Lys270	Thr274	0.12	0.15
Ala119	Thr123	0.19	0.17	Ile277	Thr281	0.11	0.15
Glu122	Val206	0.09	0.17	Ile278	Tyr326		0.24
Asp130	Tyr141	0.22		Met279	Thr283		0.20
Tyr132	Thr136		0.13	Trp286	Asn318		0.09
Tyr132	Glu225	0.09		Asn293	Tyr308	0.29	0.22
Leu144	Lys149	0.22		Val295	Gln299		0.14
Val157	Ser161	0.13	0.20	His296	Asn301	0.08	
Val160	Thr164		0.20	Asn312	Adr343	0.24	0.27
Ser161	Ser165	0.18	0.21	Asn318	Asn322		0.22
Thr164	Tyr199	0.21	0.14	Asn322	Tyr326	0.19	
Pro168	Trp173	0.24		Arg328	Arg333		0.20
Pro168	Tyr174	0.14		Gln337	Leu342	0.14	
Trp173	Asn196	0.09	0.16				

Table S8. Contact rates between the different residues for the inactive and active state of  $\beta_2$ AR based on 7 snapshots from the trajectory. The rates are given in  $\text{ps}^{-1}$ . The residue IDs start at 1.

Residues				Residues				Residues			
Residues		Rates		Residues		Rates		Residues		Rates	
Res 1	Res 2	Inactive	Active	Res 1	Res 2	Inactive	Active	Res 1	Res 2	Inactive	Active
Asp29	Val33		0.02	Ile135	Gln243	0.01		Ser236	Asp251		0.07
Glu29	Lys97		0.04	Thr136	Gln229		0.02	Ser236	Arg253	0.07	
Gly37	Ser41	0.22	0.17	Pro138	Gln142		0.05	Ser236	Arg260		0.04
Ile47	Asn51	0.15	0.16	Lys140	Gln243	0.05		Glu237	Arg253	0.10	0.05
Asn51	Ser319	0.13	0.12	Tyr141	Glu268	0.10		Glu237	Arg260	0.26	0.09
Val52	Thr56	0.21	0.19	Ser143	Lys149		0.04	Gly238	Asn244		0.03
Ala57	Phe61		0.21	Lys147	Arg151	0.05		Arg239	Asn244		0.02
Ala57	Gln65	0.03		Val157	Ser161	0.10	0.14	Arg239	His256	0.02	
Ile58	Gln65	0.15	0.11	Val160	Thr164	0.16	0.19	Arg239	Arg259	0.12	
Arg63	Asp331		0.15	Ser161	Ser165	0.14	0.22	Arg239	Arg260	0.07	
Arg63	Glu338	0.14		Thr164	Tyr199		0.18	Phe240	Thr254	0.03	
Leu64	Asn69	0.13	0.08	Pro168	Trp173	0.03		His241	Gly252	0.06	
Gln65	Tyr70		0.02	Pro168	Tyr174	0.09	0.07	Val242	Gln250	0.08	
Thr68	Asp130	0.19	0.03	Trp173	Asn196	0.08	0.10	Val242	Gly252	0.01	
Asn69	Thr73	0.18	0.18	Tyr174	Asn196	0.11	0.10	Gln243	Glu249	0.07	
Asn69	Tyr326	0.08		Arg175	Asn196	0.07	0.09	Asn244	Val248	0.12	
Tyr70	Ser74	0.11		Ala176	Tyr185	0.05		Gln247	Arg253		0.03
Tyr70	Ala150	0.07		Ala176	Phe194	0.12	0.20	Val248	Arg253		0.02
Asp79	Ser120		0.06	His178	Val297		0.02	Glu249	Arg253		0.21
Asp79	Ser319	0.06		Gln179	Asn183	0.03	0.02	Gln250	Arg260		0.08
Asp79	Asn322		0.05	Asn183	Gln187	0.05		Gln250	Thr254	0.05	0.10
Val86	Trp109	0.21	0.22	Tyr185	Phe194	0.17	0.14	Gly255	Arg259		0.03
Gly90	Trp313	0.09		Asp192	Lys305	0.17	0.22	Arg253	Arg260		0.03
His93	Met98	0.01		Phe193	Lys305	0.03		Gly255	Arg260		0.04
His93	Cys191	0.12	0.07	Gln197	Ile294		0.04	Gly257	Leu266		0.03
Lys97	Glu306	0.05		Tyr199	Ser203	0.08	0.15	Arg259	Lys263		0.02
Trp99	Thr189	0.05	0.07	Ala200	Ser204	0.21	0.20	Arg259	Phe264		0.03
Asn103	Glu107		0.02	Ser203	Ser207	0.12		Arg259	Cys265	0.01	
Asn103	Tyr185	0.12		Tyr209	Phe290	0.17	0.17	Cys265	His269	0.08	
Asn103	Ala186		0.02	Val216	Ser220	0.15	0.17	Lys267	Asp331	0.09	
Asn103	Gln187	0.06		Tyr219	Leu272	0.15		Lys270	Thr274		0.05
Asn103	Glu188	0.06		Arg221	Glu225		0.14	Lys270	Arg328	0.02	
Cys106	Thr110	0.24	0.24	Glu225	Gln229	0.15	0.28	Lys270	Asp331	0.03	
Glu107	Ser111	0.18	0.18	Lys227	Gln231	0.04		Ile277	Thr281	0.14	0.15
Glu107	Gln170		0.03	Lys227	Glu268		0.13	Ile278	Tyr326		0.04
Glu107	His172	0.07	0.15	Arg228	Glu249	0.25		Met279	Thr283	0.18	0.15
Glu107	Tyr174	0.27		Gln229	Ser262	0.09		Thr281	Asn318		0.09
Glu107	Arg175	0.35	0.07	Gln229	Lys263	0.06		Trp286	Asn318		0.06
Asp113	Asn312	0.01		Leu230	Arg239	0.16		Phe289	Asn293	0.02	
Asp113	Tyr316	0.27	0.26	Gln231	Arg239	0.03		Phe289	Tyr308	0.03	
Val114	Thr118	0.17	0.19	Gln231	Phe240	0.02		Asn293	Tyr308	0.03	0.24
Cys116	Ser120	0.20	0.07	Gln231	His241	0.02		Val295	Gln299		0.02
Ala119	Thr123	0.24	0.24	Gln231	Glu268		0.04	His296	Asn301	0.02	
Glu122	Ser161	0.02		Lys232	Gln250		0.02	His296	Ile303	0.01	
Glu122	Val206		0.20	Lys232	Ser262		0.11	Gly315	Ser319	0.19	
Asp130	Tyr141		0.04	Ile233	Gly238	0.06		Tyr316	Gly320	0.03	
Asp130	Ser143	0.20		Asp234	Arg239	0.18		Asn318	Asn322	0.15	0.16
Arg131	Tyr141	0.02		Asp234	Gln250		0.02	Leu324	Arg328		0.16
Arg131	Gln142	0.14		Asp234	Arg253		0.30	Cys327	Arg333	0.18	
Tyr132	Thr136	0.06	0.16	Asp234	Thr254		0.03	Arg328	Arg333		0.20
Phe133	Ser137	0.14		Asp234	Arg260	0.08	0.11	Ser329	Arg333		0.03
Ala134	Tyr141	0.02		Lys235	Arg260		0.03	Arg333	Gln337	0.09	
Ile135	Gln229	0.12		Ser236	Gln250		0.14	Gln337	Leu342	0.16	0.02



Table S9. Rates of the contacts formed between the ligand adrenaline and  $\beta_2$ AR for the active and the inactive state using 7 frames from the trajectory. The rates are given in  $\text{ps}^{-1}$ .

Residues		Rates	
Res 1	Res 2	Inactive	Active
Adr	Asp113	0.29	0.24
Adr	Ser203	0.02	
Adr	Asn312	0.14	0.15

Table S10. Secondary structure rates for the active and the inactive state of  $\beta_2$ AR based on 7 snapshot from the simulation trajectory. The rates are given in  $\text{ps}^{-1}$ .

Sec. Struct.		Rates	
Sec 1	Sec 2	Inactive	Active
N-Term	ECL1		0.04
TM1	TM7	0.13	0.12
ICL1	H8	0.14	0.15
TM2	TM3	0.40	0.31
TM2	TM4	0.07	
TM2	ECL2	0.12	0.06
TM2	TM7	0.23	0.05
ECL1	ECL2	0.05	0.07
ECL1	TM7	0.05	
TM3	TM4	0.02	0.03
TM3	ECL2	0.92	0.24
TM3	TM5	0.12	0.20
TM3	ICL3	0.01	0.02
TM3	TM7	0.28	0.26
ICL2	ICL3	0.05	
ICL2	TM6	0.10	
TM4	TM5		0.18
ECL2	TM6		0.02
ECL2	TM7	0.20	0.22
TM5	TM6	0.32	0.34
TM6	TM7	0.06	0.44
TM6	ICL4	0.02	
TM6	H8	0.11	
TM7	H8	0.18	

## II. SUPPLEMENTARY FIGURES

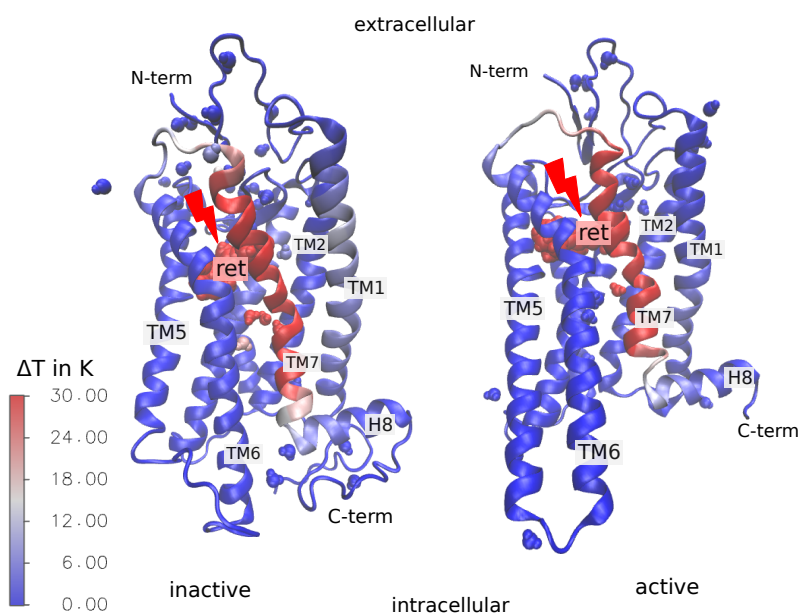


Figure S1. Rhodopsin shown in the inactive and active state including water molecules 10 ps after heating the retinal. The water molecules are depicted as spheres.

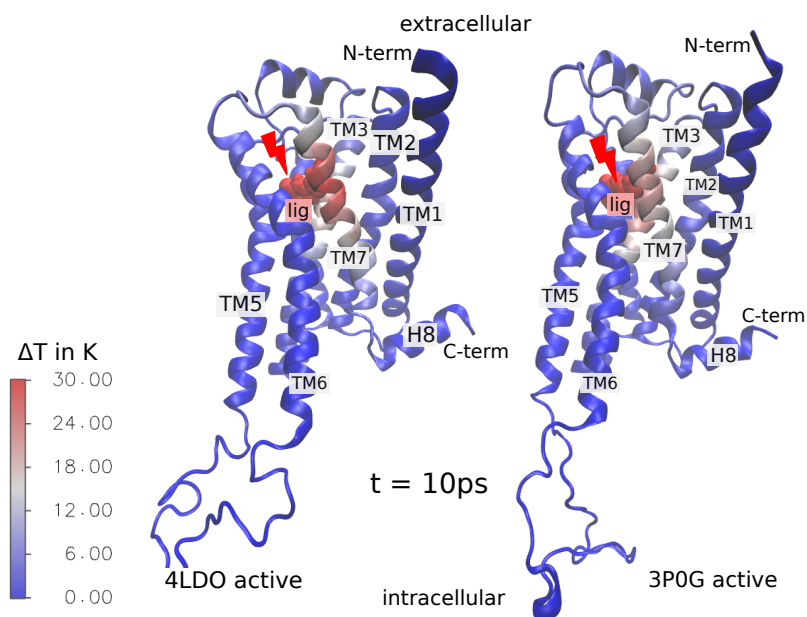


Figure S2. The two active states of  $\beta_2AR$  (4LDO on the left and 3P0G on the right side) shown 10 ps after heating the ligand.

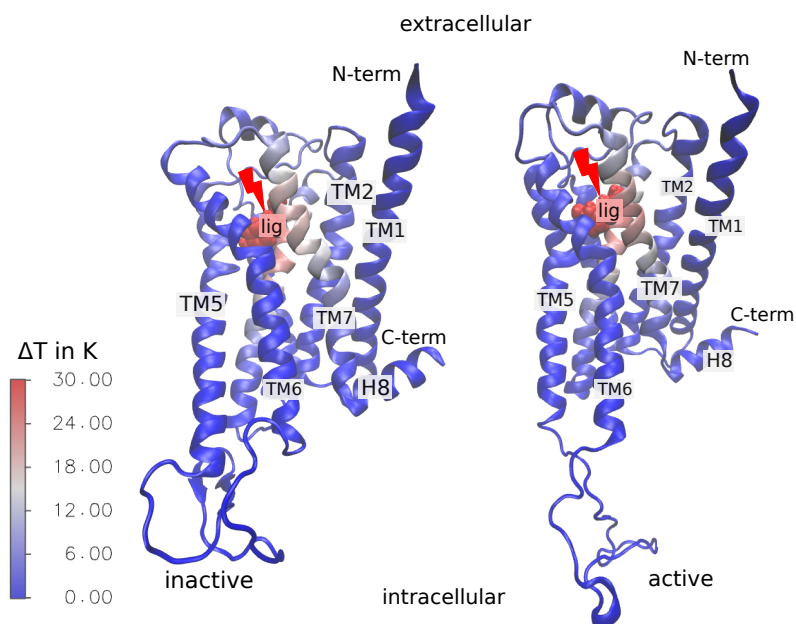


Figure S3.  $\beta_2$ AR shown in the inactive and active state 10 ps after heating the ligand. The results are based on the contacts computed from 7 snapshots from the simulation trajectory.